First-principles investigation of ferromagnetism and ferroelectricity in bismuth manganite

Nicola A. Hill
Materials Department, University of California, Santa Barbara, California 93106-5050

Karin M. Rabe
Department of Applied Physics, Yale University, P.O. Box 208284, New Haven, Connecticut 06520-8284

(Received 22 September 1998)

We present results of local spin density approximation (LSDA) pseudopotential calculations for the perovskite structure oxide, bismuth manganite ($BiMnO_3$). The origin of the differences between bismuth manganite and other perovskite manganites is determined by first calculating total energies and band structures of the high symmetry cubic phase, then sequentially lowering the magnetic and structural symmetry. Our results indicate that covalent bonding between bismuth cations and oxygen anions stabilizes different magnetic and structural phases compared with the rare earth manganites. This is consistent with recent experimental results showing enhancement of charge ordering in doped bismuth manganite. [S0163-1829(99)11113-5]

I. INTRODUCTION

Perovskite structure oxides exhibit a wide range of low-temperature structural distortions associated with lattice instabilities of the prototype cubic structure (Fig. 1), including ferroelectric (e.g., $PbTiO_3$ and $BaTiO_3$), antiferroelectric (e.g., $PbZrO_3$), and antiferrodistortive (e.g., $SrTiO_3$). Both first- and second-order transitions are observed, with a full spectrum of transition behavior ranging from displacive to order-disorder. The strong coupling between the electric polarization and the structural distortions has led to the widespread use of perovskites such as lead zirconium titanate (PZT) in piezoelectric transducer and actuator applications.[1]

In *magnetic* perovskites, different microscopic orientations of the spin-polarized ions give rise to different macroscopic magnetic symmetries. This results in rich phase diagrams, in which both the magnetic order and the structure depend on the temperature, pressure, and chemical composition. A large amount of recent research activity[2] has been focused on the rare earth perovskite-structure manganites, following the observation of colossal magnetoresistance (CMR) in Ca-doped $LaMnO_3$.[3] During these recent studies, many rare earth perovskite manganites have been found to show strong coupling between their magnetic and structural, or magnetic and electronic order parameters. For example, a magnetically induced structural phase transition has been observed in $La_{0.83}Sr_{0.17}MnO_3$ (Ref. 4) indicating strong coupling between the local magnetic spin moments and the lattice structure. In $Nd_{0.5}Sr_{0.5}MnO_3$, strong coupling between the magnetic spin moments and the electronic charge carriers was demonstrated when an electronic metal-insulator transition was induced by an external magnetic field.[5] The large change in conductivity with applied magnetic field, which gives these materials potential technological importance as the read element in magnetic recording heads,[6] is believed to originate from a similar type of phase transition.[7]

Materials which have strong coupling between *all three* of the magnetic, electric, and structural order parameters, resulting in simultaneous ferromagnetism, ferroelectricity, and ferroelasticity, are known as multiferroics. Most multiferroic materials are complex structures with many atoms per formula unit, and more than one formula unit per unit cell. The large number of interionic interactions has prevented isolation of the essential factors causing multiferroicity. As a result, the origin of multiferroism and the nature of the coupling between the magnetic, electric polarization, and structural order parameters are not well understood. In spite of the lack of fundamental understanding, a number of device applications have been suggested for multiferroic materials including multiple state memory elements, electric field controlled ferromagnetic resonance devices, and variable transducers with either magnetically modulated piezoelectricity or electrically modulated piezomagnetism.[9] Also, the ability to couple with *either* the magnetic *or* the electric polarization offers an extra degree of freedom in the design of conventional actuators, transducers, and storage devices.

Bismuth manganite can be regarded as the ''hydrogen atom'' of multiferroics. Although information about $BiMnO_3$ is sparse,[8] indications are that it is simultaneously ferromagnetic and ferroelectric at low temperatures, and, because it has a simple structure, it is amenable to detailed study using first-principles techniques. Investigation of $BiMnO_3$ permits the study of the essentials of multiferroism without the problems associated with simulating compounds containing many

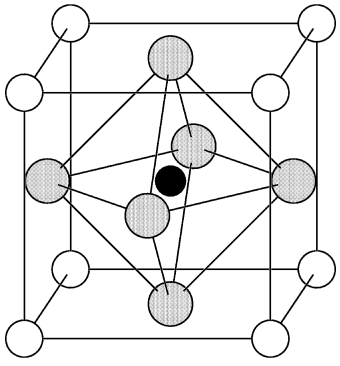

FIG. 1. The perovskite structure. The small *B* cation (in black) is at the center of an octahedron of oxygen anions (in gray). The large *A* cations (white) occupy the unit cell corners.

atoms per formula unit. In addition, $BiMnO_3$ is strikingly different, both magnetically and structurally, from the rare earth perovskite manganites. $BiMnO_3$ is ferromagnetic with a triclinic structural distortion in its ground state, whereas the rare earth manganites are antiferromagnetic and either orthorhombic or hexagonal. The differences are unexpected because bismuth and the rare earths all form trivalent cations with similar ionic radii. The anomalous behavior of $BiMnO_3$ compared with conventional perovskite manganites could give rise to unusual and useful transport properties.

The goal of the study described in this paper is to determine the origin of the differences between $BiMnO_3$ and the other perovskite manganites, both to understand the fundamental physics, and to assist in the optimization of perovskite manganite materials for novel device applications. To achieve this goal we evaluate electronic and magnetic properties of perovskite manganites using a plane wave pseudopotential (PWPP) implementation of density functional theory (DFT) within the local spin density approximation (LSDA). Our choice of theoretical approach is influenced by successful first-principles studies of *nonmagnetic* perovskite ferroelectrics.[10,11] The origin of ferroelectricity in the prototypical ferroelectric perovskites $PbTiO_3$ and $BaTiO_3$, and the reasons for the differences between them, were deduced using first principles density functional theory (DFT) calculations.[12,11] It was shown in both cases that Ti $3d$-O $2p$ hybridization is essential for ferroelectricity. In $BaTiO_3$, the Ba^{2+} ions are almost entirely ionically bonded, resulting in a rhombohedral structure. In $PbTiO_3$, however, the Pb $6s$ electrons are partially covalently bonded with the oxygen $2p$ electrons, favoring a tetragonal structure.

Throughout this work, we use $LaMnO_3$ as our example of a typical rare earth manganite, and compare our calculated results for $BiMnO_3$ with those for $LaMnO_3$. Since Bi is adjacent to Pb, near the right-hand side of the periodic table, and La is adjacent to Ba on the left-hand side, we anticipate by analogy with the earlier $PbTiO_3$-$BaTiO_3$ study, that the high lying occupied Bi $6s$ electrons will contribute to the structural and magnetic differences between $BiMnO_3$ and $LaMnO_3$. In addition we will find significant hybridization between the Bi $6p$ and O $2p$ electrons.

The remainder of this paper is organized as follows. In Sec. II we describe the plane wave pseudopotential LSDA implementation of density functional theory which we use for this study. Our PWPP implementation is shown to give results which are in excellent agreement with previously published all electron calculations for magnetic perovskite oxides. In Sec. III our results for $BiMnO_3$ and $LaMnO_3$ are presented. Our results are summarized in Sec. IV.

II. COMPUTATIONAL TECHNIQUE

The calculations described in this work were performed using a plane wave pseudopotential implementation[13] of density functional theory[14] within the local spin density approximation. Plane wave basis sets offer many advantages in total energy calculations for solids, including completeness, an unbiased representation, and arbitrarily good convergence accuracy. They also allow for straightforward mathematical formulation and implementation, which is essential in the calculation of Hellmann-Feynman forces[15] and in density functional perturbation theory calculations.[17]

However, plane wave basis sets necessitate the use of pseudopotentials to model the electron-ion interaction, in order to avoid rapid oscillations of the valence wave functions in the region around the ion cores. The accuracy and efficiency of *ab initio* pseudopotential calculations (compared with all electron calculations) is now well established for nonmagnetic systems,[18] but application of the method to spin-polarized magnetic systems is still in its infancy. Traditionally, magnetic materials containing transition metals have been studied using all electron methods with mixed basis sets, such as the linear augmented plane wave (LAPW),[19] linear muffin tin orbital,[20] or Korringa-Kohn-Rostoker[21] approaches.

Resistance to the use of the PWPP method to study these systems has been based on two perceived difficulties.

(1) First, the magnetic properties of the transition metals and their compounds originate from tightly bound d electrons, which might be expected to require a prohibitively large number of plane waves to expand their pseudopotentials. This problem can be overcome by using the optimized pseudopotentials developed by Rappe *et al.*[22] Optimized pseudopotentials minimize the kinetic energy in the high Fourier components of the pseudo wave function, leading to a corresponding reduction in the contribution of high Fourier components in the solid. The use of optimized pseudopotentials reduces the energy cutoff of the plane wave expansion in transition metal solids to around 60 Ry or less.

(2) Second, implicit within the pseudopotential approximation is the assumption that the exchange-correlation potential V_{xc} is separable into a valence part and a core part:

$$V_{xc}(\rho,\sigma)=[V_{xc}(\rho,\sigma)-V_{xc}(\rho^v,\sigma^v)]+V_{xc}(\rho^v,\sigma^v). \quad (1)$$

Here ρ is the electron density, σ is the spin polarization, and the superscript v refers to the contribution from the valence electrons. If the core electrons are spatially separated from the valence electrons then this separation is rigorously correct. However, in transition metals, the d electrons have large wave function amplitudes near the core region. Therefore, because V_{xc} is a nonlinear function of both charge and spin polarization, use of Eq. (1) is inaccurate. Early pseudopotential calculations for magnetic materials attempted to circumvent this problem by using a small core radius.[23,24] This resulted in a pseudo wave function which was similar to the all electron wave function and therefore could not be expanded efficiently using plane waves. A better solution is offered by the partial nonlinear core correction scheme of Louie *et al.*,[25] in which the core charge density is explicitly retained in both the construction of the ionic pseudopotential, and in the DFT calculation.

The PWPP method with optimized pseudopotentials and partial nonlinear core corrections was first tested by Sasaki *et al.* for ferromagnetic nickel and iron.[26] The structural and magnetic properties calculated using the PWPP method were found to be in excellent agreement with results from all electron calculations. A similar study using different soft pseudopotentials obtained comparable results for the ground-state properties of nickel.[27] More recently, Lewis and co-workers presented the first PWPP calculation for a magnetic *compound* (CrO_2),[28] and showed that the results agreed well with those of all electron LSDA calculations. Before present-

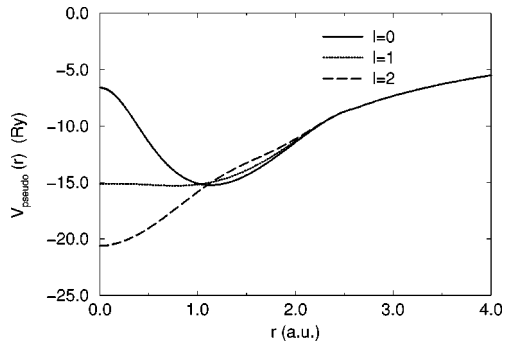

FIG. 2. Optimized ionic pseudopotentials for La. The core radius is 2.6 a.u. for all angular momenta. Four basis functions were included in the optimization, which used a cutoff wave vector of 7.5 a.u.

ing our results for $BiMnO_3$ in Sec. III, we will compare the results of our PWPP calculations for a magnetic *perovskite* with published all-electron calculations[29] and show that similarly good agreement is obtained.

A. Pseudopotential construction

For La and Bi, we constructed optimized scalar-relativistic pseudopotentials, using (for La) a $5s^2 5p^6 5d^1$ reference configuration with core radius $(r_c)=2.6$ a.u., and (for Bi) a $6s^{0.5}6p^{1.2}6d^{0.3}$ reference configuration with $r_c=3.0$ a.u. In the La reference configuration the $4f$ orbitals were unoccupied, and for Bi the filled $4f$ shell was placed in the core. The pseudopotentials were optimized using four basis functions with a cutoff wavevector q_c of 7.5 a.u. q_c determines the convergence of the kinetic energy with respect to the plane wave cutoff energy in reciprocal space calculations. The resulting optimized pseudopotentials are shown in Figs. 2 and 3. The pseudopotentials were tested for transferability by comparing with all electron calculations for a range of typical atomic and ionic configurations. The pseudoeigenvalues and total energies are equivalent to the all electron values to within a few meV.

For Mn and O we constructed non-relativistic optimized pseudopotentials. The oxygen pseudopotentials were generated from a $2s^2 2p^4$ reference configuration with core radii of 1.5 a.u. for both *s* and *p* orbitals. They were then optimized using four and three basis functions with q_c of 7.0 and 6.5 a.u. for *s* and *p* orbitals, respectively. The oxygen pseudopotentials were used in earlier calculations for nonmagnetic perovskite oxides[10] and gave accurate results. For Mn, a $4s^{0.75}4p^{0.25}3d^5$ reference configuration was used, with r_c equal to 2.0, 2.15, and 2.0 a.u. for *s*, *p*, and *d* orbitals. The optimized pseudopotentials for Mn were constructed using four basis functions and $q_c=7.5$ a.u., and partial nonlinear core corrections[25] were included. The core charge was approximated by a zeroth order spherical Bessel function within a radius of 0.737 a.u., with the full core charge used outside this radius. The resulting optimized pseudopotentials are shown in Figs. 4 and 5. Again the pseudopotentials are transferable to within a few meV.

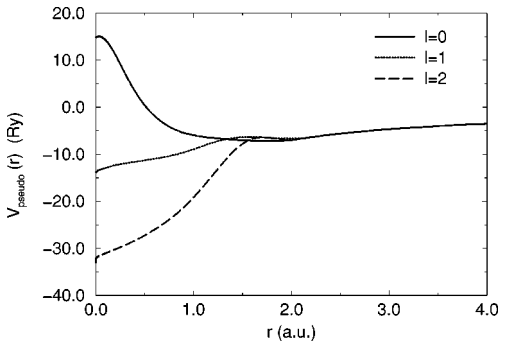

FIG. 4. Optimized ionic pseudopotentials for Mn. The exchange-correlation potential contribution from the core charge has been subtracted, in accordance with the nonlinear core correction scheme of Louie *et al.* (Ref. 25). The core radii are 2.0, 2.15, and 2.0 a.u., respectively, for the *s*, *p*, and *d* pseudopotentials. Four basis functions were included in the optimization, which used a cutoff wave vector of 7.5 a.u.

All pseudopotentials were put into separable form[30] using two projectors for each angular momentum.[31] The first projector was taken as the atomic pseudo wave function, and the second projector as r^2 times the first projector, suitably orthogonalized to the first.[32] For La, Bi, and Mn, the $l=0$ component was chosen as the local potential. For oxygen the local potential was the $l=1$ component. The absence of

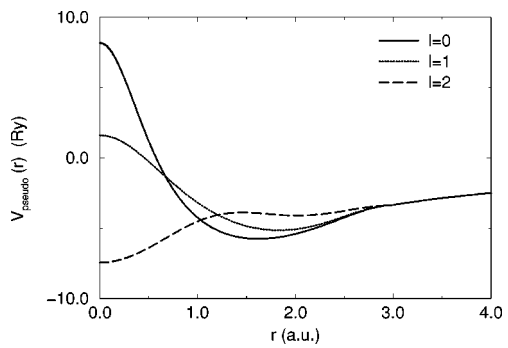

FIG. 3. Optimized ionic pseudopotentials for Bi. The core radius is 3.0 a.u. for all angular momenta. Four basis functions were included in the optimization, which used a cutoff wave vector of 7.5 a.u.

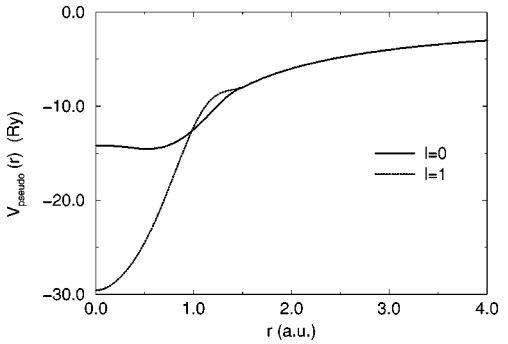

FIG. 5. Optimized ionic pseudopotentials for oxygen. The core radius is 1.5 a.u. The *s* pseudopotential was optimized using four basis functions and a cutoff wave vector of 7.0 a.u., and the *p* pseudopotential used three basis functions and a cutoff wave vector of 6.5 a.u.

ghost states was confirmed using the ghost theorem of Gonze, Käckell, and Scheffler.[33]

B. Technical details

The total energy and band structure calculations were performed on a Silicon Graphics Power Challenge L using the conjugate gradient program CASTEP 2.1 (Refs. 34,35) which we have extended to study spin-polarized systems. We used a plane wave cutoff of 60 Ry, which corresponds to around 3500 plane waves in a cubic unit cell with lattice constant of around 4 Å. A variable Gaussian broadening between 1 and 0.002 eV was applied to the *k*-point sampling to speed convergence for metallic systems. A $6\times6\times6$ Monkhorst-Pack[36] grid was used for all calculations. This led to 10*k* points in the irreducible Brillouin zone for the high symmetry cubic structures, and a correspondingly higher number for the distorted structures with lower symmetry.

The Perdew-Zunger parametrization[37] of the Ceperley-Alder exchange correlation potential[38] with the von Barth-Hedin interpolation formula[39] was used. Previous all-electron calculations for perovskite manganites[29] found no appreciable difference between results obtained using the von Barth-Hedin and the more sophisticated Vosko-Wilk-Nusair[40] interpolations.

For density of states (DOS) calculations we interpolated the calculated eigenvalues to a grid of $\approx350\,000$ *k* points in the irreducible simple cubic Brillouin zone using the interpolation scheme of Monkhorst and Pack.[36] We then applied the Gilat-Raubenheimer method[41] to this fine mesh. Finally, for the band structure plots, and for use in the tight-binding analysis, symmetry labels along high-symmetry lines were assigned using projection operators for the corresponding irreducible representations.

C. Comparison with LAPW calculations

Before presenting our new results for $BiMnO_3$, we first show that the results obtained for perovskite manganites using this PWPP implementation are in excellent agreement with the results of previously published LAPW calculations. Figure 6 shows the band structures for up- and down-spin electrons in cubic ferromagnetic $CaMnO_3$, calculated in this work using the PWPP method. We used a ten electron Ca pseudopotential with a $3s^2 3p^5 3d^1$ Ca^{2+} reference configuration and core radii of 1.29, 1.29, and 1.45 a.u. for the *s*, *p*, and *d* potentials. Four basis functions were included in the optimization,[22] with a cutoff wavevector of 7.0 a.u. The band structures are indistinguishable from those shown in Fig. 7 of Ref. 29, which were calculated using the LAPW method. In addition, we find that our PWPP calculated energy difference between the ferromagnetic and paramagnetic phases of $CaMnO_3$ is 876 meV, within 2% of the LAPW value of 860 meV. The inclusion of nonlinear core corrections is essential. The pseudopotential band structure calculated *without* nonlinear core corrections is markedly different from the LAPW band structure. In particular the energy of the minority spin Mn 3*d* bands is too high, a pseudogap opens up in the majority spin O 2*p* bands, and the lower O 2*p* bands have unphysical flat regions. In addition the total energy difference between the ferromagnetic and paramagnetic phases is overestimated to be 3.2 eV.

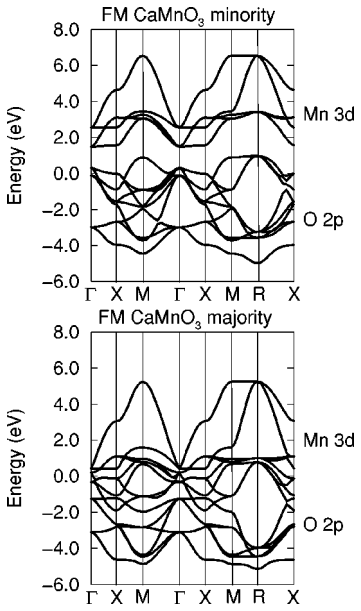

FIG. 6. Up- and down-spin band structures for $CaMnO_3$ calculated using the plane wave pseudopotential method and the partial nonlinear core correction method of Louie *et al.* (Ref. 25). The band structures are in good agreement with earlier LAPW calculations (Ref. 29).

III. CALCULATED ELECTRONIC PROPERTIES OF $BiMnO_3$ AND $LaMnO_3$

In this section we investigate the origin of the differences between $BiMnO_3$ and the rare earth manganites by comparing the calculated electronic properties of $BiMnO_3$ with those of $LaMnO_3$. We begin by calculating the electronic structure for the high symmetry cubic phases, without including magnetic effects, then lower the magnetic symmetry to the ferromagnetic phase. Finally we introduce structural distortions in both paramagnetic and ferromagnetic calculations. This ability to isolate structural and magnetic distortions is unique to computational studies, and allows identification of the essential microscopic interactions which cause

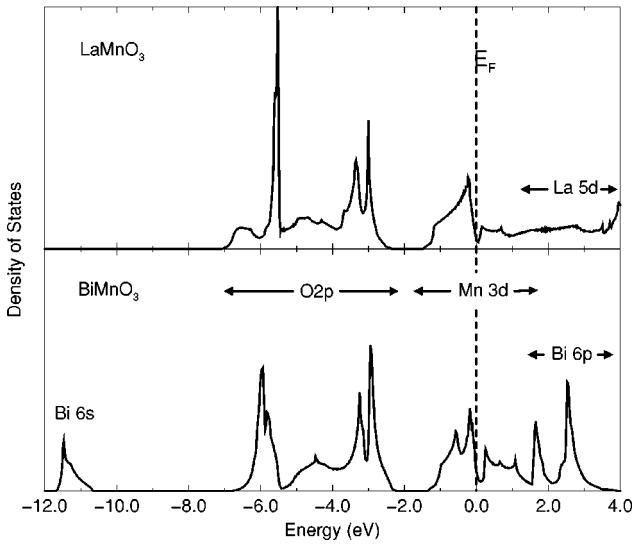

FIG. 7. Calculated densities of states for cubic paramagnetic $LaMnO_3$ and $BiMnO_3$.

the observed macroscopic behavior. All calculations are carried out at the experimental lattice constant of 3.95 Å.

A. Cubic paramagnetic structures

First we present results for $BiMnO_3$ and $LaMnO_3$ in the highest possible symmetry state—that is the cubic structure, without spin polarization [we call this the paramagnetic (PM) phase]. Although this phase is experimentally inaccessible, it provides a useful reference for understanding the ferromagnetic (FM) structures to be discussed later in this paper.

Figure 7 shows the calculated densities of states for cubic paramagnetic $LaMnO_3$ and $BiMnO_3$. The plotted energy range is from -12 to 4 eV, and the lower lying semicore states have been omitted for clarity. The Fermi level is set to zero in both cases. The broad series of bands between -2 and -7 eV in both materials arises from the oxygen $2p$ orbitals. Above the oxygen $2p$ bands, and separated from them by an energy gap, are the Mn $3d$ bands. The Mn $3d$ bands are divided into two sub-bands—the lower energy t_{2g} bands and the higher energy e_g bands—as a result of crystal field splitting by the octahedral oxygen anions. One striking *difference* between the two DOS plots is the presence of a band between -10 and -12 eV in the $BiMnO_3$ band structure which does not exist in the $LaMnO_3$ case. This band corresponds to the high lying occupied Bi $6s$ electrons. In addition, the high-energy La $5d$ electrons have a very different form than the Bi $6p$ electrons, which occupy a similar energy range.

The Fermi level lies near the top of the Mn $3d$ t_{2g} bands and is in a region of high density of states. The large DOS at the Fermi level suggests that the cubic PM structure is unstable, and that a lower-energy structure could be achieved by allowing spin-polarization and/or structural distortion.

Figure 8 shows the corresponding band structures along the high symmetry axes of the simple cubic Brillouin zone. Again the broad O $2p$ bands between -2 and -7 eV can be seen clearly in both materials, with the Mn $3d$ bands above them, separated by an energy gap. The highlighted lines in the band structure plots accentuate the upper and lower Mn $3d$ bands, which have a similar form to each other and to those of $CaMnO_3$ (Fig. 6). This indicates a ''universality'' in the manganite structure throughout the perovskite manganite series, which is independent of the identity of the large cation.

Again we observe the Bi $6s$ band, which can be seen to have considerable dispersion suggesting that it is involved in covalent bonding. In addition, the Mn $3d$ bands in $BiMnO_3$ overlap with the partially occupied Bi $6p$ orbitals, whereas in $LaMnO_3$ the next highest bands are the unoccupied La $5d$ bands.

The differences between the two band structures show up clearly in the bands along the $\Gamma \rightarrow X$ line. This region of the band structure is shown in Fig. 9 with the symmetry labels added, and the energy scale extended to include the lower energy O $2s$ and La $5p$ bands. In the following discussion we focus on the bands with Δ_1 symmetry as capturing the essential features. The Δ_1 bands are plotted with solid lines, and all other bands with dashed lines.

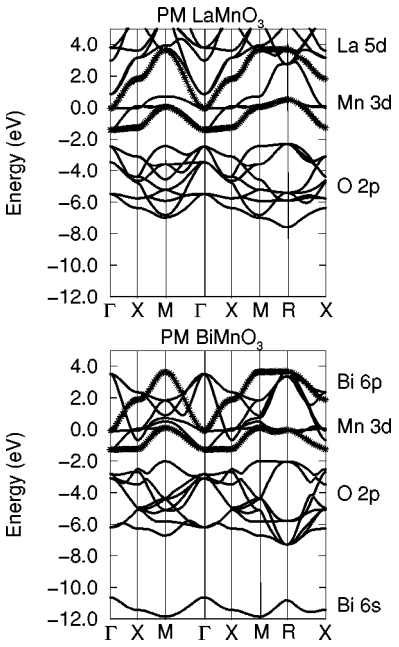

FIG. 8. Calculated band structures for cubic paramagnetic $LaMnO_3$ and $BiMnO_3$ along the high symmetry axes of the Brillouin zone. The highlighted lines in the band structure plots accentuate the upper and lower Mn $3d$ bands, which have a similar form to each other and to those of $CaMnO_3$ (Fig. 6).

In $LaMnO_3$, the oxygen $2p\Delta_1$ bands decrease monotonically in energy from Γ to X, and the Mn $3d$ Δ_1 band increases monotonically from Γ to X. Figure 10 shows a contour plot of the charge density in the group of bands above the O $2p$ manifold near the Fermi level at the Γ point. The spacing of the outer three lines is $\frac{1}{3}$ that of the innermost contours. The charge density has been projected on the (100) plane by integrating through the whole unit cell perpendicular to (100). The Mn ion is located at the center of the plot, the La ions at the corners and the O ions in the middle of the cell edges and at the center. It is clear that the Fermi surface consists largely of Mn $3d$ electrons, with contributions from

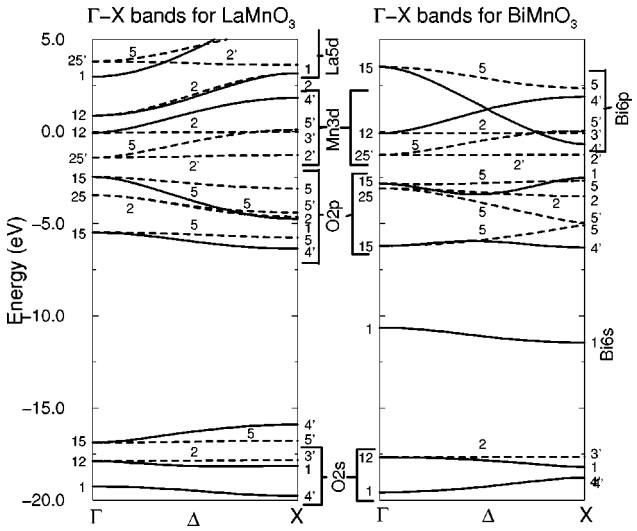

FIG. 9. Calculated band structures for cubic paramagnetic $LaMnO_3$ and $BiMnO_3$ along the $\Gamma \rightarrow X$ axis. The solid lines show the bands of Δ_1 symmetry.

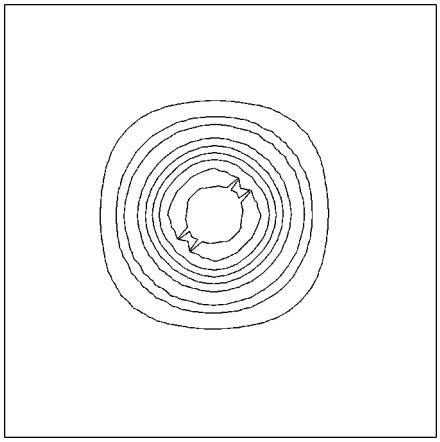

FIG. 10. Contour plot of the charge density distribution in the Mn $3d$ bands at the Γ point of $LaMnO_3$. A (100) projection is shown, with the Mn cation at the center of the square, the La ions at the corners, and the oxygen anions at the edge midpoints and the center. The charge density has been integrated through the unit cell perpendicular to the (100) plane.

other atoms below the resolution of the plot. The charge density at the X point is very similar, except that there is a small oxygen contribution, indicating that the amount of Mn $3d$-O $2p$ hybridization increases along the Γ to X line.

In $BiMnO_3$ the behavior is quite different. First, the X_1 symmetry of the Bi $6s$ band at the X point causes the X_1 O $2p$ band to be ''pushed up'' in energy, resulting in a different ordering of the O $2p$ bands at the X point. The Mn $3d$ Δ_1 band crosses the very dispersive Bi $6p$ Δ_1 band, and the latter moves below the Fermi level near the X point. Figures 11 and 12 show contour plots at the Γ and X points, respectively, of the charge density in the five bands near the Fermi level above the O $2p$ manifold. (These are the bands which we found to be entirely Mn $3d$ in the case of $LaMnO_3$.) Again the charge density is projected onto the (100) plane, and the same scale is used for the contours as in

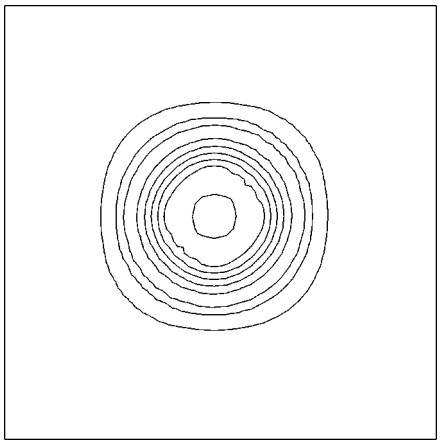

FIG. 11. Contour plot of the charge density distribution in the Mn $3d$ bands at the Γ point of $BiMnO_3$. A (100) projection is shown, with the Mn cation at the center of the square, the Bi ions at the corners, and the oxygen anions at the edge midpoints and the center. The charge density has been integrated through the unit cell perpendicular to the (100) plane. Note the similarity to the corresponding plot for $LaMnO_3$ (Fig. 10).

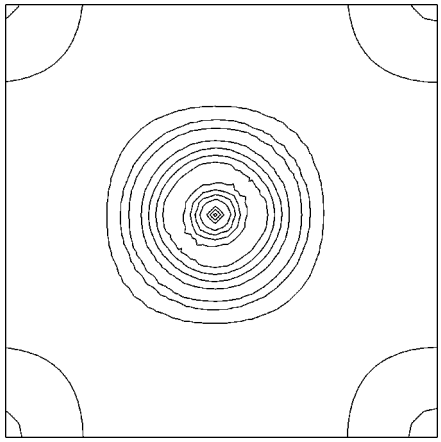

FIG. 12. Contour plot of the charge density distribution in the ''Mn $3d$'' bands at the X point of $BiMnO_3$. A (100) projection is shown, with the Mn cation at the center of the square, the Bi ions at the corners, and the oxygen anions at the edge midpoints and the center. The charge density has been integrated through the unit cell perpendicular to the (100) plane.

Fig 10. At the Γ point the charge distribution is similar to that of $LaMnO_3$. However, at X there is a significant amount of charge density around the Bi atoms. Further analysis reveals that the Bi component is in the X_4' band, which crossed the highest Mn $3d$ band. The lack of anticrossing between the Bi $6p$ and Mn $3d$ Δ_1 bands is due to the zero matrix element between the Bi $6p$ and Mn $3d$ orbitals.

To quantify the differences between cubic PM $BiMnO_3$ and $LaMnO_3$, we performed tight-binding analyses of the Γ to X regions of the respective band structures. Tight-binding parameters were obtained by non-linear-least-squares fitting[43] to the calculated *ab initio* energies at the high symmetry Γ and X points, and at 19 points along the Δ axis. First we performed analyses with only oxygen $2s$ and $2p$ and Mn $3d$ orbitals included in the basis set. The tight-binding parameters thus obtained are given in Table I. The band energies calculated using these parameters have root mean square (rms) deviations from the *ab initio* energies of 0.20 for $LaMnO_3$ and 0.25 for $BiMnO_3$. The resulting band structures for the bands of Δ_1 symmetry are compared with the *ab initio* values in Fig. 13. The limited basis set reproduces the $LaMnO_3$ bands well, consistent with an early proposal by Goodenough[42] that the magnetic properties of $LaMnO_3$ are determined by the Mn $3d$-O $2p$ hybridization only. Note that the fit to the lower energy O $2s$ bands is the least good—these bands are very close in energy to the La $5p$ bands which have not been included in the fit. The behavior of the $BiMnO_3$ Δ_1 bands is less well reproduced, confirming that additional orbital overlaps are essential in producing the observed band structure.

We then repeated the fitting procedure for $BiMnO_3$, with Bi $6s$ and $6p$ orbitals added to the basis. Transfer integrals between nearest neighbor Bi $6s$-O $2p$, Bi $6p$-O $2p$, Bi $6p-$Mn $3d$, and Bi $6p$-Bi $6p$ orbitals were allowed to be nonzero. This significantly improved the quality of the fit to the *ab initio* bands (see Fig. 14), and reduced the root mean square deviation to 0.12. The values of the new tight-binding parameters are given in Table II. The largest transfer integrals involving Bi are the Bi $6s$-O $2p$ and Bi $6p$-O $2p$ σ

TABLE I. Tight-binding parameters for $BiMnO_3$ and $LaMnO_3$ obtained by non-linear-least-squares fitting to the *ab initio* eigenvalues along Γ to X. E indicates an orbital energy and V an interatomic transfer integral. All transfer integrals are between nearest neighbors, except those with the subscript 2 which are between next nearest neighbors. Only the parameters listed in the table were allowed to be nonzero in the fitting procedure.

	$BiMnO_3$	$LaMnO_3$
E_{O2s}	−17.680595	−17.836376
E_{O2p}	−3.444399	−4.514022
E_{Mn3d}	−1.202430	−1.191285
$V_{O2s\text{-}O2s}$	−0.252108	−0.243683
$V_{(O2p\text{-}O2p)\sigma}$	0.735211	0.620568
$V_{(O2p\text{-}O2p)\pi}$	−0.132201	−0.063466
$[V_{(O2p\text{-}O2p)\sigma}]_2$	−0.211935	0.182635
$[V_{(O2p\text{-}O2p)\pi}]_2$	−0.044754	0.082951
$V_{O2s\text{-}Mn3d}$	−1.720688	−1.735814
$V_{(O2p\text{-}Mn3d)\sigma}$	−1.964201	−1.838490
$V_{(O2p\text{-}Mn3d)\pi}$	1.036316	0.878961
$V_{(Mn3d\text{-}Mn3d)\delta}$	−0.003391	0.066346

interactions, with the magnitude of the σ-bonded Bi $6p$-O $2p$ interaction being approximately 30% larger than that of the Bi $6s$-O $2p$. Also large are the Bi $6p$-Bi$6p$ σ interactions, which cause the Bi $6p\Delta_1$ band to be pushed down below the Fermi level.

B. Comparison with experiment

The conclusion from our tight-binding analysis is consistent with recent measurements showing enhancement of charge ordering in Bi-doped $CaMnO_3$.[45] Rao and coworkers observed that the charge-ordered state in $Bi_{0.3}Ca_{0.7}MnO_3$ persists to a higher temperature than that in

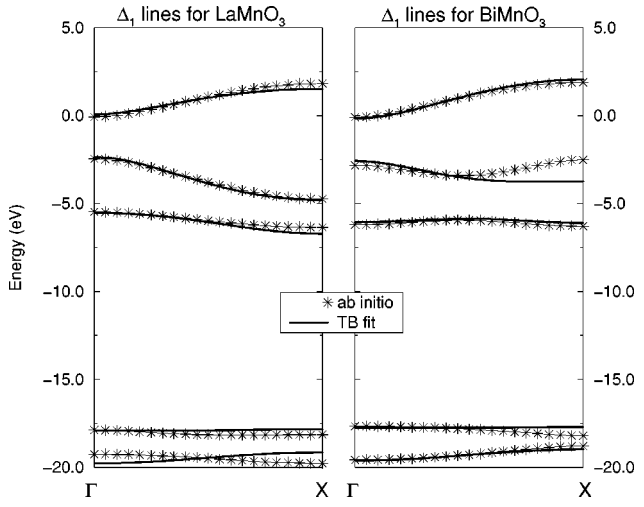

FIG. 13. Comparison of *ab initio* Δ_1 bands with those obtained from a tight-binding fit using only Mn and O orbitals in the basis. The fit for $LaMnO_3$ is good indicating that only the Mn and O ions are significantly involved in covalent bonding. The fit for $BiMnO_3$ has a higher rms deviation, and in particular misses the additional curvature around −3 eV near the X point. This shows that additional interactions are present.

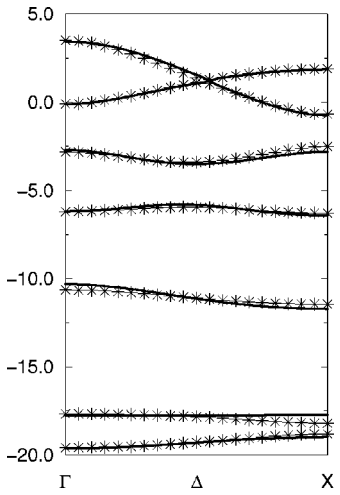

FIG. 14. Comparison of *ab initio* Δ_1 bands with those obtained from a tight-binding fit including Bi $6s$ and $6p$ orbitals in addition to Mn $3d$ and O $2s$ and $2p$. The fit is improved over the fit using only Mn and O orbitals.

$La_{0.3}Ca_{0.7}MnO_3$. They explained their observations by noting that the electronegativity of Bi enhances Bi-O hybridization and in turn reduces the amount of Mn-O hybridization.

Additional evidence in support of this phenomenon can be extracted from Ref. 46, in which a temperature-composition phase diagram for $Bi_{1-x}Ca_xMnO_3$, showing the charge-ordered transition and the Néel temperature, is plotted. Com-

TABLE II. Tight-binding parameters for $BiMnO_3$ obtained by non-linear-least-squares fitting to the *ab initio* eigenvalues along Γ to X. An expanded tight-binding basis including the Bi $6s$ and $6p$ orbitals was used. The labeling scheme for the parameters is the same as in Table I. Only the parameters shown were allowed to be nonzero.

	$BiMnO_3$
E_{Bi6s}	−10.310688
E_{Bi6p}	0.202695
E_{O2s}	−17.717958
E_{O2p}	−3.725773
E_{Mn3d}	−1.167871
$V_{Bi6p\text{-}Bi6p\sigma}$	0.848443
$V_{Bi6p\text{-}Bi6p\pi}$	0.166061
$V_{Bi6s\text{-}O2p}$	−0.812502
$V_{(Bi6p\text{-}O2p)\sigma}$	−1.061660
$V_{(Bi6p\text{-}O2p)\pi}$	−0.145201
$V_{(Bi6p\text{-}Mn3d)\sigma}$	0.170850
$V_{(Bi6p\text{-}Mn3d)\pi}$	0.078144
$V_{O2s\text{-}O2s}$	−0.237506
$V_{(O2p\text{-}O2p)\sigma}$	0.652059
$V_{(O2p\text{-}O2p)\pi}$	−0.125450
$[V_{(O2p\text{-}O2p)\sigma}]_2$	−0.010196
$[V_{(O2p\text{-}O2p)\pi}]_2$	−0.002797
$V_{O2s\text{-}Mn3d}$	−1.645508
$V_{(O2p\text{-}Mn3d)\sigma}$	−1.926533
$V_{(O2p-Mn3d)\pi}$	0.959768
$V_{(Mn3d\text{-}Mn3d)\delta}$	0.029347

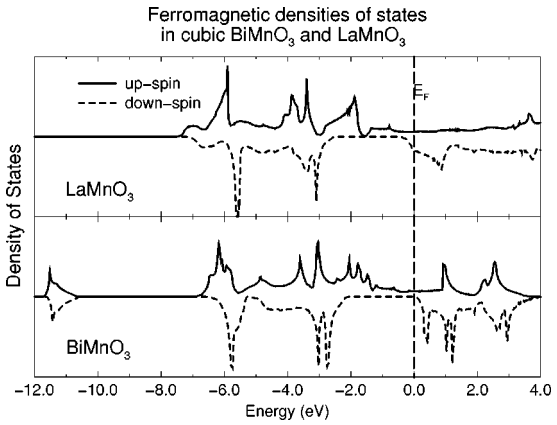

FIG. 15. Calculated densities of states for cubic ferromagnetic $LaMnO_3$ and $BiMnO_3$.

parison with similar data for $La_{1-x}Ca_xMnO_3$ (in, for example, Ref. 47) confirms that the charge ordered phase persists to higher temperature in Bi-doped $CaMnO_3$ than in La-doped $CaMnO_3$. The ability to tune the positions of phase boundaries by substitution of Bi for the rare earth ions might prove valuable in optimizing materials properties for specific device applications.

C. Cubic ferromagnetic structures

Next, we present the results of calculations in which the high symmetry cubic structure is retained, but the electrons are allowed to spin polarize. We find that introduction of spin polarization reduces the energy of both $BiMnO_3$ and $LaMnO_3$ by around 1 eV per unit cell compared with the paramagnetic case. The most important observation of this section is that the *differences* between $BiMnO_3$ and $LaMnO_3$ which we observed in the paramagnetic calculations persist

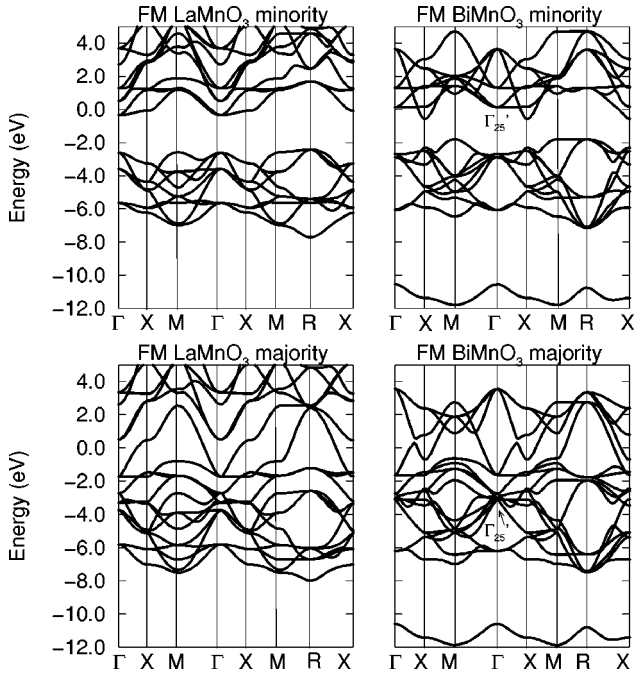

FIG. 16. Up- and down-spin band structures for cubic $LaMnO_3$ and $BiMnO_3$ along the high symmetry axes of the Brillouin zone.

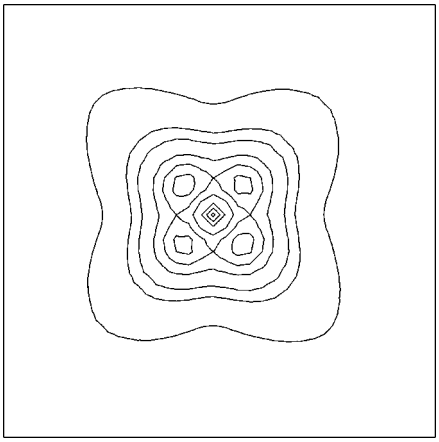

FIG. 17. Minority conduction band charge density in cubic FM $LaMnO_3$. The charge density is projected on the (001) plane of the cubic unit cell.

into the ferromagnetic phase, the PM to FM transition introducing the same kinds of changes in both materials.

Figure 15 shows the calculated densities of states for cubic ferromagnetic $LaMnO_3$ and $BiMnO_3$. The majority spins are represented by the solid line on the positive y axis, and the minority spins by the dashed line on the negative y axis. In both $LaMnO_3$ and $BiMnO_3$, the down-spin Mn $3d$ band is split off from the O $2p$ band, and has a similar form to the corresponding paramagnetic band. The up-spin Mn $3d$ hybridizes strongly with the O $2p$ and there is no band gap for the majority carriers. The up-spin DOS at the Fermi level in $LaMnO_3$ is still high, indicating that the cubic FM state has a high energy. This is consistent with the fact that the lowest-energy spin polarization in *structurally relaxed* $LaMnO_3$ is antiferromagnetic.[44] The DOS at the Fermi level in $BiMnO_3$

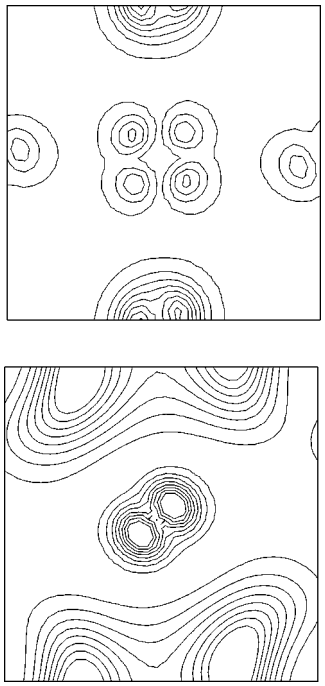

FIG. 18. Minority conduction band charge density in cubic FM $BiMnO_3$. The upper plot is a (100) slice through the Mn-O plane, and the lower plot is a (100) slice through the Bi-O plane.

TABLE III. Force constant matrices in cubic paramagnetic $BiMnO_3$ and $LaMnO_3$.

	$BiMnO_3$						$LaMnO_3$				
	Bi	Mn	O*z*	O*x*	O*y*		La	Mn	O*z*	O*x*	O*y*
Bi	−5.47	−2.37	−0.73	4.28	4.28	La	−0.05	−2.64	−0.71	1.70	1.70
Mn	−2.46	11.12	−8.66	0.00	0.00	Mn	−3.07	15.10	−11.57	−0.21	−0.21
O*z*	−0.64	−8.57	13.03	−1.91	−1.91	O*z*	−0.72	−11.53	17.04	−2.40	−2.40
O*x*	4.28	−0.09	−1.82	−2.19	−0.18	O*x*	1.92	−0.46	−2.38	−0.01	0.91
O*y*	4.28	−0.09	−1.82	−0.18	−2.19	O*y*	1.92	−0.46	−2.38	0.91	−0.01

is somewhat lower suggesting that the FM phase should be more stable in $BiMnO_3$ than in $LaMnO_3$. For both compounds, the Fermi level cuts through the very bottom of the down-spin Mn 3*d* bands, and the conduction band is occupied almost entirely by up-spin electrons. Materials in which the electrons at the Fermi level are 100% spin polarized are known as half-metallics, and are considered desirable for use in devices such as spin transistors. Again the most obvious differences between the two electronic structures are the presence of the Bi 6*s* band between −10 and −12 eV, and the contrasting forms of the Bi 6*p* and La 5*d* bands.

Figure 16 shows the up and down-spin band structures for $BiMnO_3$ and $LaMnO_3$ along the high symmetry axes of the simple cubic Brillouin zone. There are many similarities between the FM and PM energy bands, and our earlier conclusions regarding the origins of the differences between $BiMnO_3$ and $LaMnO_3$ continue to be valid.

First we examine the up- and down-spin $LaMnO_3$ band structures, and compare with the PM $LaMnO_3$ band structures to determine the changes which spin polarization causes in a ''conventional'' manganite. The states which correspond to nonmagnetic atoms are unchanged from the paramagnetic state, and are identical for up- and down-spin electrons. For example, the dispersion of the lowest O 2*p* band is identical for up and down spin, and for the PM phase. Also the La 5*d* bands, which were above the Mn 3*d* bands in the PM state are unchanged in form and energy. The characteristic perovskite manganite Mn 3*d* pattern which we remarked on earlier persists in the FM phase, appearing around 2 eV higher for the down-spin electrons than for the up-spin because of the exchange splitting. The up-spin Mn 3*d* and O 2*p* bands are strongly hybridized and there is no gap between them. However, the down-spin Mn 3*d* are split off from the O 2*p* bands by a larger gap than in the PM case. As a result, the Mn 3*d* bands occupy the same energy region as the unoccupied La 5*d* bands.

Next we compare the up- and down-spin $BiMnO_3$ band structures. As expected, the nonmagnetic Bi 6*s* band and the lower O 2*p* bands are identical for up and down spin. In fact the overall form of the *down-spin* O 2*p* bands is almost identical to that of the corresponding PM $BiMnO_3$ bands. However, it is different from that of the down spin $LaMnO_3$ O 2*p* bands—in particular the structure at the Γ point is quite different, a consequence of the unusual behavior of the Δ_1 band which we observed earlier in the PM bands. Both up- and down-spin Mn 3*d* bands show the characteristic perovskite manganite features (most noticeable in this case along the *M*-*R*-*X* directions) which we noted earlier in our discussions of the PM band structures, and of $CaMnO_3$. The form of the down-spin Mn 3*d*/Bi 6*p* bands is similar to that of the PM phase, although the energy separation from the O 2*p* bands is larger. In contrast, the majority bands show strong hybridization between the Mn 3*d* and O 2*p* electrons. The lowest Mn 3*d* bands at the Γ point (Γ'_{25}) move below the upper O 2*p* bands. At the *R* point, the Bi 6*p* bands are now above the Mn 3*d* bands, whereas in the down-spin and paramagnetic band structures they were below.

The contrast between the $BiMnO_3$ and $LaMnO_3$ minority conduction electrons is striking. Figure 17 is a contour plot of the small amount of down spin charge density in the region above, and separated by a gap from, the O 2*p* bands. The charge density through the entire unit cell has been projected onto the (100) plane. The electrons are localized entirely in the Mn 3*d* orbitals with no hybridization with the O atoms. This is a result of the large energy separation between the Mn and O bands, which in turn is a consequence of the minority Mn 3*d* bands being pushed to higher energy by exchange forces. There is no contribution from the La atoms, because the La 5*d* electrons never intersect the Fermi level. Figure 18 shows the charge density of the down-spin conduction band electrons in $BiMnO_3$. Rather than summing over the unit cell, two different slices through the unit cell are shown. The upper plot is in the Mn-O (100) plane, with the Mn ion at the center and O ions at the edge midpoints. There is minority spin conduction band charge density local-

TABLE IV. Eigenvectors and eigenvalues of the dynamical matrix which correspond to the unstable phonon modes in cubic paramagnetic $BiMnO_3$ and $LaMnO_3$.

	$BiMnO_3$						$LaMnO_3$				
ν (cm^{-1})	Bi	Mn	O*z*	O*x*	O*y*	ν (cm^{-1})	La	Mn	O*z*	O*x*	O*y*
72.39*i*	0.0	0.0	0.0	$-\frac{1}{\sqrt{2}}$	$\frac{1}{\sqrt{2}}$	49.04*i*	0.0	0.0	0.0	$-\frac{1}{\sqrt{2}}$	$\frac{1}{\sqrt{2}}$
98.20*i*	−0.43	0.09	0.16	0.62	0.62	44.69*i*	−0.59	0.22	0.21	0.53	0.53

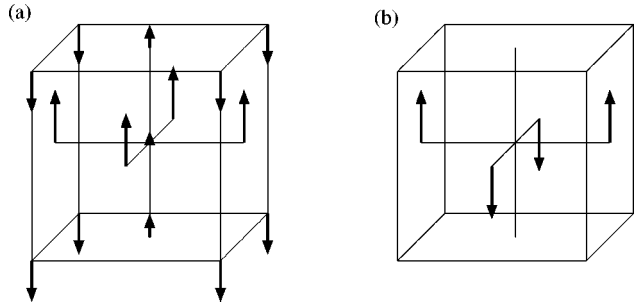

FIG. 19. Eigenvectors of the two unstable Γ point phonon modes in $BiMnO_3$. The Mn ion is at the center of the unit cell surrounded by an octahedra of oxygens, with the Bi ions at the unit cell corners. Each mode is threefold degenerate. (a) is the mode which leads to a ferroelectric distortion; (b) is a nonferroelectric mode.

ized on both the Mn and O ions. The lower plot is in the Bi-O (100) plane, with Bi ions at the corners and an O ion at the center. We see that the Bi contribution to the charge density is both large and highly directional. The fact that the conduction electrons partly occupy *p*-type atomic orbitals should produce quite different transport characteristics than those observed in conventional rare earth manganites, where the conduction bands are entirely Mn $3d$ type.

D. Ferroelectric distortions

Finally we investigate the origin of the proposed ferroelectricity in $BiMnO_3$. In keeping with the philosophy of this paper, we study the lattice distortions of the high symmetry cubic phases, and compare our results for $BiMnO_3$ with those for $LaMnO_3$. We restrict our discussion to zone center phonons.

The perovskite manganites have five atoms per unit cell, which results in 15 phonon branches, 3 acoustical and 12 optical. At the Γ point all phonons are threefold degenerate, so there is one acoustical phonon frequency (which is zero), and four optical frequencies. We are interested in the optical phonons which have negative eigenvalues, indicating lattice instabilities.

The force constant matrices for $LaMnO_3$ and $BiMnO_3$ were determined by calculating the Hellmann-Feynman forces resulting from the displacement of each atom in turn 0.1 Å along the *z* direction of the unit cell. The forces exerted on the Mn ions by the other ions were determined using the acoustic sum rule. We calculated the Mn-Mn force by applying the acoustic sum rule to both the columns and the rows of the resulting matrix. The two values differed by less than around 0.001 eV/Å . Our calculated force constant matrices for paramagnetic $LaMnO_3$ and $BiMnO_3$ are tabulated in Table III.

The paramagnetic cubic phases of both $LaMnO_3$ and $BiMnO_3$ have two unstable phonon modes. The frequencies and eigenvectors of the unstable modes are given in Table IV. The mode involving motion of the equatorial oxygens, shown in Fig. 19(b), does not correspond to a ferroelectric distortion and will not be discussed further. The displacement pattern for the second unstable mode is shown in Fig. 19(a). Here the large (Bi or La) cations are moving in opposition to the oxygen cage, resulting in a ferroelectric displacement. The imaginary frequency of this mode is twice as large in $BiMnO_3$ than in $LaMnO_3$, indicating a stronger instability in the Bi compound. It is interesting to note that the Mn is moving in the same direction as the oxygen ions. This is opposite to the behavior of the Ti ion in $BaTiO_3$ and $PbTiO_3$, but similar to the behavior of Zr in $PbZrO_3$.[16]

The imaginary frequency phonons in the ferromagnetic phases are less unstable than the corresponding imaginary frequency paramagnetic phonons. In fact the ferroelectric mode in $LaMnO_3$ is now only slightly unstable, at $21.1i$ cm^{-1}, and the other formerly unstable mode now has a positive frequency. However, the frequency of the ferroelectric mode in ferromagnetic $BiMnO_3$ remains strongly unstable, at $82.30i$ cm^{-1}.

It is clear from our analysis, that the presence of ferroelectricity in $BiMnO_3$, and absence of ferroelectricity in $LaMnO_3$, can be explained by the different zone center lattice instabilities. Although a definitive prediction requires calculation of the phonon dispersion throughout the entire Brillouin zone, it is likely that the weakly unstable zone center phonon in $LaMnO_3$ will be overshadowed by a stronger instability elsewhere in the Brillouin zone, reproducing theoretically the experimentally observed Jahn-Teller distortion. Similarly, the very unstable ferroelectric mode at the zone center in $BiMnO_3$ is likely to dominate over possible unstable modes at other frequencies, confirming theoretically the suggested existence of ferroelectricity in $BiMnO_3$. We are in the process of developing spin-polarized density functional perturbation theory code[17] which will allow us to investigate efficiently the nature of the phonons throughout the entire Brillouin zone. Our results will be the subject of a future publication.

An alternative suggestion for the origin of the ferroelectricity in $BiMnO_3$ is that it originates from an electronic phase transition, in contrast to the conventional displacive ferroelectricity caused by a lattice distortion.[48] Such *electronic ferroelectricity* has been demonstrated theoretically[49] in the insulating phase of the Falicov-Kimball model, and there is some experimental data which is consistent with the occurrence of electronic ferroelectricity.[49] The correlations associated with the electronic instability are included via a BCS-like wave function and thus the resulting energy is not expected to be well described within the local density approximation. In similar situations, however, LDA results have been successfully used to compute values of model parameters for input to many-body investigations.[50] This is clearly a subject which merits further experimental and theoretical study.

IV. SUMMARY

Our results indicate that covalent bonding between the bismuth cations and oxygen anions in $BiMnO_3$ introduces additional orbital interactions compared with the rare earth manganites, in which the rare earth—oxygen interaction is essentially purely ionic. These additional orbital interactions in turn stabilize different magnetic and structural phases. Our results are consistent with the limited experimental data on doped $BiMnO_3$-based compounds, and suggest that a modern experimental study of pure $BiMnO_3$ might reveal novel and potentially useful phenomena.

ACKNOWLEDGMENTS

The authors acknowledge many useful discussions with Umesh Waghmare, Eric Cockayne, Serdar Öğüt, and Steven Lewis. We thank the authors of CASTEP for providing us with their software package, and Umesh Waghmare for implementing the extension to metallic systems. Funding for this work was provided by Hewlett Packard Laboratories and by the Office of Naval Research, Contract No. N00014-91-J-1247. We thank Professors C.N.R. Rao and Tony Cheetham for sharing their experimental results prior to publication, and Professor Lu Sham and Dr. Morrel Cohen for bringing electronic ferroelectricity to our attention. Many of the ideas presented in this manuscript were formulated during a workshop at the Aspen Center for Physics.

[1] L. E. Cross, Mater. Chem. Phys. **43**, 108 (1996).
[2] See, for example, *Proceedings of the 41st Annual Conference on Magnetism and Magnetic Materials*, Atlanta, GA, 1996 [J. Phys. Soc. Jpn. **81**, 8 (1997)], and references therein.
[3] S. Jin, T. H. Tiefel, M. McCormack, R. A. Fastnacht, R. Ramesh, and L. H. Chen, Science **264**, 413 (1994).
[4] A. Asamitsu, Y. Moritomo, Y. Tomioka, L. Arima and Y. Tokura, Nature (London) **373**, 407 (1995).
[5] H. Kuwahara, Y. Tomioka, A. Asamitsu, Y. Moritomo, and Y. Tokura, Science **270**, 961 (1995).
[6] J. A. Brug, T. C. Anthony, and J. H. Nickel, MRS Bull. **21**(9), 23 (1996).
[7] H. Kuwahara, Y. Tomioka, Y. Moritomo, A. Asamitsu, M. Kasai, R. Kumai, and Y. Tokura, Science **272**, 80 (1996).
[8] Literature searches for 1960 and later turned up only the following 5 papers: I. O. Troyanchuk, N. V. Kasper, O. Mantytskaya, and S. N. Pastushonok, JETP **78**, 212 (1994); I. O. Troyanchuk and V. N. Derkachenko, Sov. Phys. Solid State **32**, 1436 (1990); Y. Y. Tomashpol'skii and Y. N. Venevtsev, Sov. Phys. Crystallogr. **16**, 905 (1972); V. A. Bokov, N. A. Grigoryan, M. F. Bryzhina, and V. S. Kazaryan, Bull. Acad. Sci. USSR, Phys. Ser. **33**, 182 (1969); F. Sugawara, S. Iida, Y. Syono, and S. Akimoto, J. Phys. Soc. Jpn. **25**, 1553 (1968).
[9] V. E. Wood and A. E. Austin, in *Magnetoelectric Interaction Phenomena in Crystals*, edited by A. J. Freeman and H. Schmid (Gordon and Breach, New York, 1975).
[10] U. V. Waghmare and K. M. Rabe, Phys. Rev. B **55**, 6161 (1997).
[11] R. E. Cohen and H. Krakauer, Ferroelectrics **136**, 95 (1992).
[12] R. E. Cohen, Nature (London) **358**, 136 (1992).
[13] M. T. Yin and M. L. Cohen, Phys. Rev. B **26**, 5668 (1982).
[14] H. Hohenberg and W. Kohn, Phys. Rev. **136**, B864 (1964); W. Kohn and L. J. Sham, *ibid.* **140**, A1133 (1965).
[15] P. Bendt and A. Zunger, Phys. Rev. Lett. **50**, 1684 (1983).
[16] Ph. Ghosez, E. Cockayne, and K.M. Rabe (unpublished).
[17] X. Gonze, Phys. Rev. B **55**, 10 337 (1997).
[18] See, for example, M. L. Cohen, Phys. Today **32**(7), 40 (1979), and references therein.
[19] D. J. Singh, *Planewaves, Pseudopotentials and the LAPW Method* (Kluwer, Norwell, MA, 1994).
[20] O. K. Anderson, Phys. Rev. B **12**, 3060 (1975).
[21] J. Korringa, Physica (Amsterdam) **13**, 392 (1947); W. Kohn and N. Rostocker, Phys. Rev. **94**, 1111 (1954).
[22] A. M. Rappe, K. M. Rabe, E. Kaxiras, and J. D. Joannopolous, Phys. Rev. B **41**, 1227 (1990).
[23] H. S. Greenside and M. A. Schluter, Phys. Rev. B **27**, 3111 (1983); **28**, 535 (1983).
[24] J. Zhu, X. W. Wang, and S. G. Louie, Phys. Rev. B **45**, 8887 (1992).
[25] S. G. Louie, S. Froyen, and M. L. Cohen, Phys. Rev. B **26**, 1738 (1982).
[26] T. Sasaki, A. M. Rappe, and S. G. Louie, Phys. Rev. B **52**, 12 760 (1995).
[27] J.-H. Cho and M.-H. Kang, Phys. Rev. B **52**, 9159 (1995).
[28] S. P. Lewis, P. B. Allen, and T. Sasaki, Phys. Rev. B **55**, 10 253 (1997).
[29] W. E. Pickett and D. J. Singh, Phys. Rev. B **53**, 1146 (1996).
[30] L. Kleinman and D. M. Bylander, Phys. Rev. Lett. **48**, 1425 (1982).
[31] P. E. Blöchl, Phys. Rev. B **41**, 5414 (1990).
[32] M. P. Teter, Phys. Rev. B **48**, 5031 (1993).
[33] X. Gonze, P. Käckell, and M. Scheffler, Phys. Rev. B **41**, 12 264 (1990).
[34] M. C. Payne, M. P. Teter, D. C. Allan, T. A. Arias, and J. D. Joannopoulos, Rev. Mod. Phys. **64**, 1045 (1992).
[35] M. C. Payne, X. Weng, B. Hammer, G. Francis, U. Bertram, A. de Vita, J. S. Lin, V. Milman, and A. Qteish (unpublished).
[36] H. J. Monkhorst and J. D. Pack, Phys. Rev. B **13**, 5188 (1976).
[37] J. P. Perdew and A. Zunger, Phys. Rev. B **23**, 5048 (1981).
[38] D. M. Ceperley and B. J. Alder, Phys. Rev. Lett. **45**, 566 (1980).
[39] U. von Barth and L. Hedin, J. Phys. C **5**, 1629 (1972).
[40] S. H. Vosko, L. Wilk, and M. Nusair, Can. J. Phys. **58**, 1200 (1980).
[41] G. Gilat and L. C. Raubenheimer, Phys. Rev. **144**, 390 (1966).
[42] J. B. Goodenough, Phys. Rev. **100**, 564 (1955).
[43] L. F. Mattheiss, Phys. Rev. B **6**, 4718 (1972).
[44] E. O. Wollan and W. C. Koehler, Phys. Rev. **100**, 545 (1955).
[45] C. N. R. Rao, A. Arulraj, and A. K. Cheetham (unpublished).
[46] W. Bao, J. D. Axe, C. H. Chen, and S.-W. Cheong, Phys. Rev. Lett. **78**, 543 (1997).
[47] P. Schiffer, A. P. Ramirez, W. Bao, and S.-W. Cheong, Phys. Rev. Lett. **75**, 3336 (1995).
[48] Lu Sham (private communication).
[49] T. Portengen, Th. Östreich, and L. J. Sham, Phys. Rev. B **54**, 17 452 (1996).
[50] M. S. Hybertsen, E. B. Stechel, M. Schluter, and D. R. Jennison, Phys. Rev. B **41**, 11 068 (1990).